To appear in *Liquid Crystals*
Vol. 00, No. 00, Month 20XX, 1–22

RESEARCH ARTICLE

Multistable Nematic Wells: Modelling Perspectives, Recent Results and New Directions

Apala Majumdar[a*] and Alexander Lewis[b]

[a]*Department of Mathematical Sciences, Claverton Down, University of Bath, BA2 7AY*; [b]*Mathematical Institute, University of Oxford, Andrew Wiles Building, Radcliffe Observatory Quarter, Woodstock Road, OX2 6GG*

(*June 2016*)

This review article is a consolidated but not exhaustive account of recent modelling and numerical work on nematic-filled square or cuboid shaped wells with planar degenerate boundary conditions. This seemingly simple geometry can be modelled with a simplistic Oseen–Frank approach or a more sophisticated two-dimensional and three-dimensional Landau–de Gennes approach. We discuss these approaches, reconcile the findings and in doing so, elucidate the complex interplay between material properties, temperature, geometry and boundary conditions in both equilibrium and non-equilibrium phenomena. We largely focus on static equilibria with some discussion on metastable or transient states of experimental relevance.

Keywords: Modelling, Oseen–Frank, Landau–de Gennes, Multistability, Well Order Reconstruction Solution

1. Introduction

Nematic liquid crystals (NLC) are the simplest and the most commonly used liquid crystals and, simply put, NLC are complex anisotropic liquids with a certain degree of long-range orientational ordering [1, 2]. Nematic molecules are typically rod-like in shape and these rod-shaped molecules move freely but tend to exhibit certain preferred directions of molecular alignment and these preferred directions lead to material anisotropy, which in turn, opens the door for optical, electromagnetic, mechanical and rheological applications [3, 4]. Research in NLC has grown tremendously over the last few decades partly because this is a fertile interdisciplinary field promising major scientific advances and partly because of widespread applications in modern industry and technology i.e. nematics form the backbone of the multi-billion dollar liquid crystal display (LCD) industry [3]. Scientists are particularly keen to understand pattern formation in confined nematic systems with emphasis on how to control pattern formation with various material, geometrical and external variables and these questions are intimately related to LCD design and optimization. This paper focuses on pattern formation in a particular nematic system: square or cuboid-shaped nematic wells with planar degenerate boundary conditions, consolidating a batch of four recent papers on this system [5–8], as well as introducing some previously unpublished work [9]. This confined nematic system is an example of a bistable or multistable system in the sense that there are at least two stable, optically contrasting experimentally observable nematic equilibria, without an external field. Bistable or multistable systems have long been of interest to applied researchers since they can, in principle, support multiple stable equilibria without external stimuli so that power is only needed to switch between the different states but not to maintain a static image and such technology,

*Corresponding author. Email: a.majumdar@bath.ac.uk

if successfully implemented, offers the promise of larger, higher resolution and more economical displays lucrative for industry.

Bistable LCDs often use a combination of complex surface morphologies and boundary treatments to stabilize multiple states, common examples being the commercially successful Zenithally Bistable Nematic Device (ZBD) [10] and the Post Aligned Bistable Nematic Device that was designed by Hewlett Packard more than 10 years ago [11, 12]. The ZBD cell comprises a layer of NLC material sandwiched between two surfaces, the top surface is flat and the bottom surface is characterized by a sinusoidal grating with both surfaces treated to induce normal/homeotropic boundary conditions i.e. the nematic molecules are preferentially anchored along the normal to the bounding surfaces. The ZBD cell is known to support at least two stable optically contrasting nematic states: (i) the defect-free Vertically Aligned Nematic (VAN) state for which the molecules tilt uniformly from the bottom grating to the top surface and the (ii) more planar Hybrid Aligned Nematic (HAN) state featured by two defects near the crest and trough of the bottom grating respectively. The VAN state is typically opaque to incident light and the HAN state is typically transparent to incident light [10, 13]. The PABN cell is a three-dimensional (3D) cell comprising of a layer of NLC sandwiched between two surfaces and we have a periodic array of rectangular 3D posts protruding out of the bottom surface, with the NLC outside the posts and between the two bounding surfaces. The top surface is subject to homeotropic boundary conditions and the bottom surface and the post surfaces are subject to planar degenerate, or tangential, boundary conditions, which simply require the nematic molecules in contact with these surfaces to be in the plane of these surfaces with no distinguished in-plane alignment i.e. all directions in the plane of the surface are equally preferred. The PABN cell is experimentally known to support at least two optically contrasting states: the opaque *tilted state* for which the molecules tilt vertically around each post and the transparent *planar* state for which the molecules are more planar around each post [11]. In [12], the authors propose a topological mechanism for the experimentally observed bistability in the PABN device i.e. the authors use topological classification schemes developed in [14] to characterize admissible nematic states in the PABN cell and this characterization suggests that the tilted and planar states belong to different topological classes and are hence, separated by a natural energy barrier which excludes any continuous switching between the two states without an external impetus.

We focus on NLC-filled square or cuboid-shaped wells in this paper, first reported experimentally and numerically in [15]. The geometry is relatively straightforward - we have a periodic array of 3D NLC-filled wells with a square or rectangular bottom cross-section and the well surfaces are treated to induce tangent or planar degenerate boundary conditions. In other words, each well has six surfaces: the top and bottom surfaces are in the xy-plane and there are four lateral surfaces, two in the xz-plane and two in the yz-plane respectively. The tangent boundary conditions imply that the nematic molecules on the top and bottom surfaces preferentially lie in the xy-plane and similar comments apply to the nematic molecules on the xz-surfaces and yz-surfaces. Therefore, nematic molecules along the edges are preferentially anchored tangent to the edges, for example, the molecules are oriented in the x-direction on the edges parallel to the x-axis etc.[5, 15]. The tangent conditions naturally create a mismatch in the molecular alignments at the well vertices and one expects to see defects or singularities near the vertices. We denote the well dimensions by (L_x, L_y, L_z) in the x, y, z directions respectively and typical well dimensions are somewhere between $(L_x, L_y, L_z) = (20, 20, 12)$ microns to $(80, 80, 12)$ microns, with the well height typically less than a third of the cross-section dimensions. In [15], the authors experimentally observe two different states: (i) the diagonal state for which the nematic molecules roughly align along one of the square diagonals on the bottom cross-section and (ii) the rotated state for which the nematic molecules roughly rotate by π radians between a pair of opposite square edges. Both states are stable without an external field and offer somewhat different optical properties. In [15], the authors numerically model this device as a two-dimensional (2D) square i.e. they model the bottom square cross-section and argue that structural variations are negligible in the vertical direction for a shallow well. They numerically reproduce the diagonal and rotated states in a 2D Landau–de Gennes (LdG) framework and the numerical modelling is in good agreement with experiments. The work

is [15] has been vigorously followed up in a batch of papers [16–18] where authors consider other polygonal geometries with mixed boundary conditions (planar and homeotropic) with a view to control pattern formation by manipulating geometry and boundary treatments and greater control promises new applications.

We review a batch of four papers and some previously unpublished work, co-authored by the first author, on the theoretical and numerical modelling of the cuboid-shaped nematic wells with tangent boundary conditions [5–9]. The work in [15] reveals the diagonal and rotated states, which may be the only relevant states for micron-scale wells but modern experimentalists are now well-placed to deal with severely confined nano-scale systems and to continuously tune boundary conditions, offering the possibility of new states with new optical properties, that may lend themselves to new applications. It is now timely to fully investigate the solution landscape in terms of geometrical parameters, boundary conditions, temperature, material parameters and external fields to identify and exploit the full potential for multistability. Indeed, recent numerical simulations suggest that square wells can support up to 81 nematic equilibria in certain parameter regimes, some of which are necessarily unstable but may yet be stable with respect to a large class of perturbations or may be relevant for transient dynamics [19]. The papers look at different modelling approaches for the NLC-filled wells and the approaches are ordered in terms of increasing detail: the Oseen–Frank (OF) approach in [6, 9], the 2D LdG approach in [5, 8] and the 3D LdG approach in [7].

In [6], the authors model the device as a square or a rectangle filled with planar nematic molecules within the OF framework [1, 2]. This is a simplistic approach which describes the nematic state by a 2D unit-vector field, parameterized by an angle, that corresponds to the average nematic alignment at every point in space. There are natural defects at the square vertices and the authors compute analytic expressions for the diagonal and rotated profiles, their OF energies and the energy estimates can be correlated with observational frequency of the different states. The authors use the energy estimates to propose a new empirical method for estimating a key material and geometry-dependent length scale - the surface extrapolation length. This idea is extended in work contained in [9] to incorporate the effect of an internal defect, allowing exploring of transitions between stable equilibria and calculation of energy barriers. In [5], the authors use a 2D LdG framework to model a square well filled with nematic material i.e. describe the nematic state by a LdG order parameter that has two degrees of freedom. This is effectively the same approach as in [15] with a systematic study of the effect of boundary conditions, encoded in terms of a surface anchoring coefficient W. They compute bifurcation diagrams for the static equilibria as a function of W, and find that rotated solutions are stable above a material and temperature-dependent critical anchoring coefficient W_c, which can be estimated numerically. In [5], the authors also introduce a concept of an optimal boundary condition which could be used for practical problems when communicated to a wider interdisciplinary audience. This is further followed up in [8] where the authors adopt the same 2D LdG model but with emphasis on optimal transition pathways between stable nematic equilibria for strong, moderate and weak anchoring regimes. A novelty of this approach is that it reveals the transition states or the unstable equilibria connecting the stable diagonal and rotated states and some transition states are reminiscent of experimental observations in [6] and, hence, are of independent interest. In [7], the authors model the 3D well within a 3D LdG framework i.e. the 3D LdG order parameter has five degrees of freedom and naturally contains more information about the both the directions of alignment and the degree of order about the preferred directions. The authors examine the effect of well-size on the static equilibria and their most significant numerical finding is the new well order reconstruction solution (WORS), that cannot be captured by previous modelling approaches. The WORS is structurally different to the diagonal and rotated solutions and, if experimentally realised, offers the potential of new mechanical and optical responses. However, the stability and, hence, observability of the WORS is subtly dependent on geometry, temperature and anchoring strength and the authors present numerical results to this effect in [7]. A lot of open questions remain about the solution landscape of this relatively simple geometry, especially with regards to the multiplicity of solutions, the interplay between different parameters, how solutions lose stability and the relevance of unstable solution branches, and we hope to investigate these

questions in the near future.

2. A Two-Dimensional Oseen–Frank Approach

The work in [6] is motivated by experiments on *fd*-viruses confined to microchambers reported in [20] for which the experimentalists observe profiles strongly reminiscent of the diagonal and rotated solutions, as well as profiles with interior defects and a uniform state with a completely uniform director profile. In [6], the authors restrict themselves to states with no interior defects, primarily focussing on the diagonal and rotated solutions, with an empirical estimate for the surface extrapolation length based on analytic energy estimates. We reproduce the main calculations from [6] in the OF framework, to illustrate the efficiency of such a simple model, and show a previously unpublished extension [9] of this model which allows us to include the effects of internal defects.

The OF theory is restricted to uniaxial nematics with constant order parameter i.e. nematic phases with a single distinguished direction of molecular alignment, described by a unit-vector $\boldsymbol{n}$, in the sense that all directions to $\boldsymbol{n}$ are physically equivalent. The modelling hypothesis is that the experimentally observed states correspond to critical points, typically minimizers of the OF energy functional:

$$I_{OF}[\boldsymbol{n}] := \iiint_{\Omega} \frac{1}{2}\left(K_1\left(\nabla\cdot\boldsymbol{n}\right)^2 + K_2\left(\boldsymbol{n}\cdot\nabla\times\boldsymbol{n}\right)^2 + K_3\left(\boldsymbol{n}\times\nabla\times\boldsymbol{n}\right)^2\right)\mathrm{d}V, \tag{1}$$

where K_1, K_2, K_3 are material-dependent elastic constants [1, 2] and surface energies are omitted. As stated above, the wells are typically shallow and, hence, the authors argue (as in [15]) that it suffices to model the nematic profile on the bottom well cross-section, $\left\{(x,y)\in\mathbb{R}^2; 0\le x\le L_x; 0\le y\le L_y\right\}$. The tangent boundary conditions require $\boldsymbol{n}$ be in the (x,y)-plane so that $\boldsymbol{n}$ can be written as

$$\boldsymbol{n} = \left(\cos\left(\theta\right), \sin\left(\theta\right), 0\right), \tag{2}$$

where θ is defined on a 2D re-scaled square or rectangle given by

$$\Omega := \left\{(x,y)\in\mathbb{R}^2 : 0\le x\le 1; 0\le y\le\lambda\right\}, \tag{3}$$

and $\lambda := \frac{L_y}{L_x}$ is the rectangular aspect ratio.

Let $\delta := 1 - \frac{K_1}{K_3}$ be a measure of the elastic anisotropy and the critical points are solutions of the associated Euler-Lagrange equations

$$\Delta\theta + \delta\left(\frac{1}{2}\sin\left(2\theta\right)\left(\theta_y^2 - \theta_x^2 + 2\theta_{xy}\right) + \theta_x\theta_y\cos\left(2\theta\right) - \theta_{xx}\sin^2\left(\theta\right) - \theta_{yy}\cos^2\left(\theta\right)\right) = 0, \tag{4}$$

subject to appropriate boundary conditions as described below.

In [6], the authors prescribe explicit Dirichlet boundary-value problems for the diagonal and rotated solutions respectively. The tangent boundary conditions require that $\boldsymbol{n}$ be oriented along $\pm\hat{\boldsymbol{x}}$ on the horizontal edges ($y=0$ and $y=\lambda$) and $\boldsymbol{n}$ be oriented along $\pm\hat{\boldsymbol{y}}$ on the vertical edges ($x=0$ and $x=1$) inducing a natural mismatch at the vertices. The diagonal state corresponds to an average diagonal alignment and there are two choices for the boundary conditions: (i) $\theta=0$ on the horizontal edges and $\theta=\frac{\pi}{2}$ on the vertical edges or (ii) $\theta=\pi$ on the horizontal edges and $\theta=\frac{\pi}{2}$ on the vertical edges . There are four rotated solutions of essentially two different types: (i) the first type for which $\boldsymbol{n}$ rotates by π radians between the horizontal edges and (ii) the second type for which $\boldsymbol{n}$ rotates by π radians between a pair of vertical edges. Therefore, the authors study three different sets of boundary conditions: (i) the D set for which $\theta=0$ on the horizontal edges

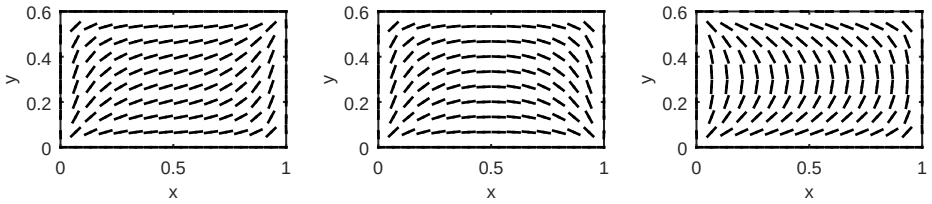

(a) The diagonal (D) state. (b) The rotated (U_1) state. (c) The rotated (U_2) state.

Figure 1. The director fields for the three equilibrium states within a rectangle with rectangular aspect ratio $\lambda = 0.6$.

and $\theta = \frac{\pi}{2}$ on the vertical edges, (ii) the U_1 set for which $\theta = 0$ on the horizontal edges, $\theta = \frac{\pi}{2}$ on $x = 0$ and $\theta = -\frac{\pi}{2}$ on $x = 1$ and (iii) the U_2 set for which $\theta = \frac{\pi}{2}$ on the vertical edges, $\theta = 0$ on $y = 0$ and $\theta = \pi$ on $y = \lambda$. Other states can be considered as rotations or reflections of these three states.

In [6], the authors work with the one-constant approximation for the OF energy, with $\delta = 0$ in (4), so that (4) reduces to the Laplace equation, $\Delta\theta = 0$, subject to Dirichlet boundary conditions on Ω. We can write an arbitrary solution of the Laplace equation subject to Dirichlet boundary conditions as the linear superposition:

$$\theta(x, y, \lambda) := a_1 f_1(x, y; \lambda) + a_2 f_2(x, y; \lambda) + a_3 f_3(x, y; \lambda) + a_4 f_4(x, y; \lambda). \tag{5}$$

The constants a_i's are determined by the Dirichlet conditions and the function f_1 is a solution of $\Delta f_1 = 0$ subject to $f_1(x, 0; \lambda) = 1$ and $f_1(0, y; \lambda) = f_1(1, y; \lambda) = f_1(x, \lambda; \lambda) = 0$. The authors define a *diagonal* solution to be of the form (5) subject to the D set of Dirichlet conditions outlined above, the U_1 *rotated solution* to be of the form (5) subject to the U_1 set of Dirichlet conditions and the U_2 *rotated solution* to be of the form (5) subject to the U_2 set of Dirichlet conditions above. The corresponding choices of $a_1, \ldots, a_4$ are enumerated in Table 1 and a straightforward computation shows that

$$\begin{aligned} f_1(x, y; \lambda) := \sum_{n=0}^{\infty} \frac{4 \sin((2n+1)\pi x)}{(2n+1)\pi} \{ & \cosh((2n+1)\pi y) \\ & - \coth((2n+1)\pi\lambda) \sinh((2n+1)\pi y) \}. \end{aligned} \tag{6}$$

The remaining functions are defined by rescaling and rotation:

$$\begin{aligned} f_2(x, y; \lambda) &:= f_1\left(\frac{y}{\lambda}, \frac{1-x}{\lambda}; \frac{1}{\lambda}\right), \\ f_3(x, y; \lambda) &:= f_1(x, \lambda - y; \lambda), \\ f_4(x, y; \lambda) &:= f_1\left(\frac{y}{\lambda}, \frac{x}{\lambda}; \frac{1}{\lambda}\right). \end{aligned} \tag{7}$$

The director fields of the three states are shown in Figure 1.

As a natural consequence of the Dirichlet conditions, there are point defects at the square vertices. These point defects have infinite energy on a two-dimensional domain [1, 2], and to allow for comparison between the energies, the authors in [6] regularize the domain Ω by removing circular arcs of radius ϵ from each corner, and evaluating the energy on the new domain denoted Ω_ϵ (shown in Figure 2). The following calculations have been reproduced from [9]. By an immediate application

Table 1. Values of the coefficients a_i for three equilibria shown in Figure 1.

State	a_1	a_2	a_3	a_4
D	0	$\pi/2$	0	$\pi/2$
U_1	0	$-\pi/2$	0	$\pi/2$
U_2	0	$\pi/2$	π	$\pi/2$

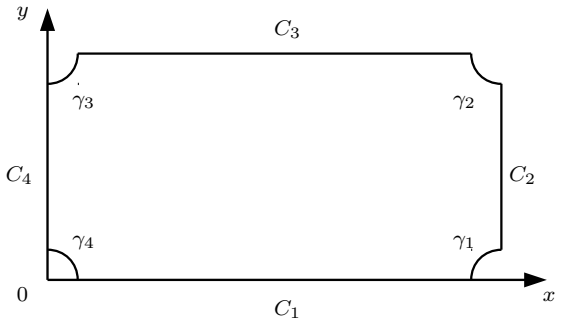

Figure 2. The boundary $\partial\Omega_\epsilon$, expressed terms of straight edges C_i and arcs γ_i.

of Green's theorem, we have

$$\begin{aligned} E[\theta] :=& \frac{K}{2}\iint_{\Omega_\epsilon} |\nabla\theta|^2 \,\mathrm{d}x\,\mathrm{d}y = \frac{K}{2}\oint_{\partial\Omega_\epsilon} \theta\frac{\partial\theta}{\partial\boldsymbol{\nu}}\,\mathrm{d}s \\ =& \frac{K}{2}\sum_{i=1}^{4}\left[\int_{C_i}\theta\frac{\partial\theta}{\partial\boldsymbol{\nu}}\,\mathrm{d}s + \int_{\gamma_i}\theta\frac{\partial\theta}{\partial\boldsymbol{\nu}}\,\mathrm{d}s\right], \end{aligned} \tag{8}$$

where $\frac{\partial\theta}{\partial\nu} = \nabla\theta\cdot\boldsymbol{\nu}$, $\boldsymbol{\nu}$ is the outward pointing unit normal to $\partial\Omega_\epsilon$, $\partial\Omega_\epsilon$ is oriented in the anti-clockwise sense and $\partial\Omega_\epsilon$ comprises 4 straight segments, denoted by C_i, and the four quarter circles around each vertex, denoted by γ_i.

The line integral about the arcs, γ_i, make an $O\left(\epsilon^2\right)$ contribution to the energy, as can be seen by considering the local solution, θ_c, near each vertex in question. For example, let the origin be a vertex; then θ_c is a solution of $\Delta\theta_c = 0$, in polar coordinates, (r,ϕ), about the origin, subject to $\theta_c(r,0) = a_1, \theta_c\left(r,\frac{\pi}{2}\right) = a_4$ and the condition, $\theta_c\left(\epsilon,\phi\right) = \theta(\epsilon\cos(\phi),\epsilon\sin(\phi))$ where θ is defined by (5). One can then show that the line integral in (8) reduces to

$$-\int_0^{\frac{\pi}{2}} \theta_c\frac{\partial\theta_c}{\partial r}\bigg|_{r=\epsilon}\epsilon\,\mathrm{d}\phi \sim -\left(a_1+a_4\right)b_1\epsilon^2 + O\left(\epsilon^4\right), \tag{9}$$

where b_1 is a matching coefficient. Further, from the definition of the functions f_i in (6)–(7), the line integrals about the straight edges, C_i, can be evaluated explicitly to show that the one-constant OF energies of all three competing states can be expressed as

$$E[\theta] \sim K\pi\left(\ln\left(\frac{1}{\epsilon}\right) + \tilde{E}_j + O\left(\epsilon^2\right)\right) \qquad j\in\{D,U_1,U_2\}. \tag{10}$$

Here the logarithmic contribution is the *defect energy* and the defect energy is identical for all three states, since they have the same number of point defects. The normalized energy, $\tilde{E}$, represents the

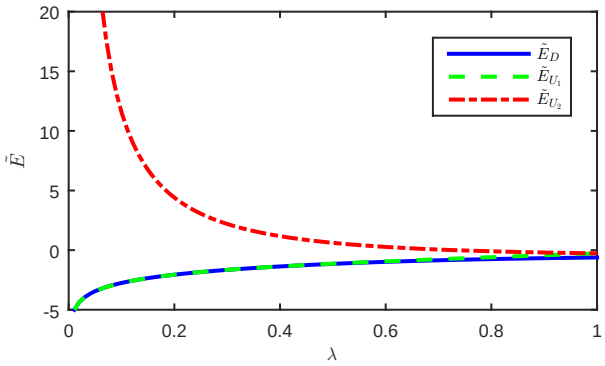

Figure 3. The normalized energies of the three equilibrium states plotted against the rectangular aspect ratio λ.

bulk distortion energy and is

$$\begin{aligned}
\tilde{E}_D &= \ln\left(\frac{2\lambda}{\pi}\right) + s_1\left(\frac{1}{\lambda}\right) - s_2\left(\frac{1}{\lambda}\right), \\
\tilde{E}_{U_1} &= \ln\left(\frac{2\lambda}{\pi}\right) + s_1\left(\frac{1}{\lambda}\right) + s_2\left(\frac{1}{\lambda}\right), \\
\tilde{E}_{U_2} &= \ln\left(\frac{2}{\pi}\right) + s_1(\lambda) + s_2(\lambda).
\end{aligned} \tag{11}$$

where the functions s_1 and s_2 are defined to be

$$\begin{aligned}
s_1(\lambda) &:= 2\sum_{n=0}^{\infty} \frac{\coth\left((2n+1)\pi\lambda\right) - 1}{2n+1} \\
s_2(\lambda) &:= 2\sum_{n=0}^{\infty} \frac{\operatorname{cosech}\left((2n+1)\pi\lambda\right)}{2n+1}.
\end{aligned} \tag{12}$$

An immediate benefit of the analytic expressions (11) is that they provide quantitative information about how λ or, equivalently, the geometrical aspect ratio manifests in energetic trends. One can immediately see that the diagonal state is energetically preferred over the rotated states for $\lambda < 1$ i.e. $\tilde{E}_D < \tilde{E}_{U_1} < \tilde{E}_{U_2}$ for $\lambda < 1$ and this is further illustrated in Figure 3. As $\lambda \to 0$, one can calculate asymptotic estimates for $s_1(\lambda)$ and $s_2(\lambda)$ to show that

$$\tilde{E}_D \sim \ln\left(\frac{2\lambda}{\pi}\right) + O\left(\exp\left[-\frac{1}{\lambda}\right]\right), \tag{13}$$

$$\tilde{E}_{U_1} \sim \ln\left(\frac{2\lambda}{\pi}\right) + O\left(\exp\left[-\frac{1}{\lambda}\right]\right), \tag{14}$$

$$\tilde{E}_{U_2} \sim \frac{\pi}{2\lambda} + \ln\left(\frac{\lambda}{2\pi}\right) + O\left(\exp\left[-\frac{1}{\lambda}\right]\right). \tag{15}$$

In other words, one cannot really distinguish between the D and U_1 states as $\lambda \to 0$ since both profiles have $\theta \approx 0$ in the square interior modulo thin transition layers near the vertical edges.

The ideas of [6] can be extended to include an internal defect of strength m located at $(x_1, y_1) \in \Omega$. This is based on previously unpublished work from [9]. The key idea is to define a solution of the Laplace equation which captures to the behaviour of the director immediately about the internal

defect:

$$h(x,y;x_1,y_1,\lambda) := m\,\mathrm{atan2}\,(a,b) \tag{16}$$

where $\mathrm{atan2}(y,x)$ is the four quadrant inverse tangent [21] and

$$a := y\cos(\phi') - x\sin(\phi') - y_1\cos(\phi') + x_1\sin(\phi'), \tag{17}$$

$$b := x\cos(\phi') + y\sin(\phi') - x_1\cos(\phi') - y_1\sin(\phi'), \tag{18}$$

$$\phi' := -\arctan\left(\frac{\lambda - y_1}{x_1}\right), \tag{19}$$

Four further functions are defined (g_i, $i = 1,\ldots,4$), which cancel out the effects of h on the four edges of Ω and also satisfy the Laplace equation. A simple calculation shows that these functions are

$$g_1(x,y;x_1,y_1,\lambda) := \sum_{n=1}^{\infty} A_n \sin(n\pi x)\left(\cosh(n\pi y) - \coth(n\pi\lambda)\sinh(n\pi y)\right), \tag{20}$$

$$g_2(x,y;x_1,y_1,\lambda) := \sum_{n=1}^{\infty} B_n \sin\left(\frac{n\pi y}{\lambda}\right)\mathrm{cosech}\left(\frac{n\pi}{\lambda}\right)\sinh\left(\frac{n\pi x}{\lambda}\right), \tag{21}$$

$$g_3(x,y;x_1,y_1,\lambda) := \sum_{n=1}^{\infty} C_n \sin\left(n\pi x\right)\mathrm{cosech}\left(n\pi\lambda\right)\sinh\left(n\pi y\right), \tag{22}$$

$$g_4(x,y;x_1,y_1,\lambda) := \sum_{n=1}^{\infty} D_n \sin\left(\frac{n\pi y}{\lambda}\right)\left(\cosh\left(\frac{n\pi x}{\lambda}\right) - \coth\left(\frac{n\pi}{\lambda}\right)\sinh\left(\frac{n\pi x}{\lambda}\right)\right), \tag{23}$$

where the Fourier coefficients A_n, B_n, C_n and D_n are

$$A_n := -2\int_0^1 h(x,0;x_1,y_1,\lambda)\sin(n\pi x)dx, \quad B_n := -\frac{2}{\lambda}\int_0^{\lambda} h(1,y;x_1,y_1,\lambda)\sin\left(\frac{n\pi y}{\lambda}\right)dy,$$
$$C_n := -2\int_0^1 h(x,\lambda;x_1,y_1,\lambda)\sin(n\pi x)dx, \quad D_n := -\frac{2}{\lambda}\int_0^{\lambda} h(0,y;x_1,y_1,\lambda)\sin\left(\frac{n\pi y}{\lambda}\right)dy. \tag{24}$$

The director field can therefore be expressed as:

$$\theta(x,y;x_1,y_1,\lambda) := h(x,y;x_1,y_1,\lambda) + \sum_{i=1}^{4}\left(a_i f_i(x,y;\lambda) + g_i(x,y;x_1,y_1,\lambda)\right), \tag{25}$$

where the functions f_i are already defined in Equations (6)–(7). Choosing suitable values of a_i, θ therefore satisfies tangent Dirichlet boundary conditions on Ω and the Laplace equation, and the director $\boldsymbol{n}$ is continuous everywhere except at the four corners of Ω and the point (x_1,y_1). Some sample director fields are shown in Figure 4, we see that the strength of one of the corner defects (here located at $(0,\lambda)$) has adjusted to accommodate the sign and strength of the internal defect. This expression for the director given in (25) can, in principle, be extended to include more internal defects by including additional terms of the form given in Equation 16 and altering the definition of the Fourier coefficients to include these extra terms.

This expression for θ can be used to evaluate the one-constant Oseen–Frank energy. Regularizing the domain by removing discs of radius ϵ centred at each of the discontinuities and introducing a

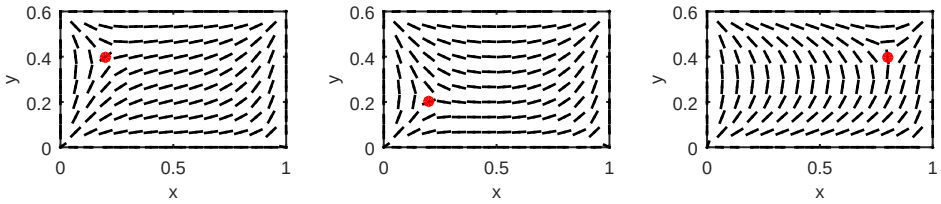

(a) $(x_1, y_1) = (0.2, 0.4)$. (b) $(x_1, y_1) = (0.2, 0.2)$. (c) $(x_1, y_1) = (0.8, 0.4)$.

Figure 4. Examples of states with internal defects of strength $m = -\frac{1}{2}$, with $\lambda = 0.6$ and $a_1 = a_3 = 0$, $a_2 = a_4 = \frac{\pi}{2}$.

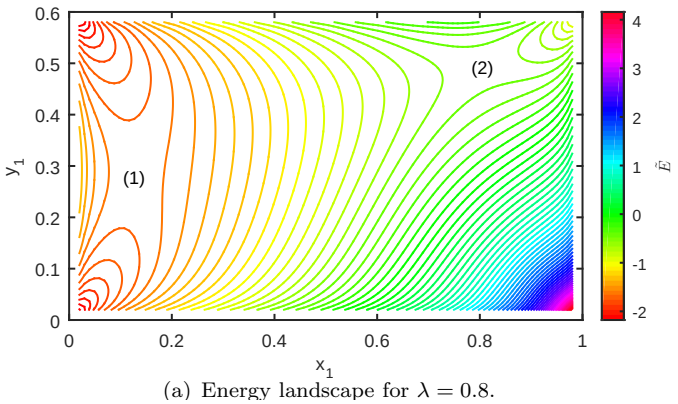

(a) Energy landscape for $\lambda = 0.8$.

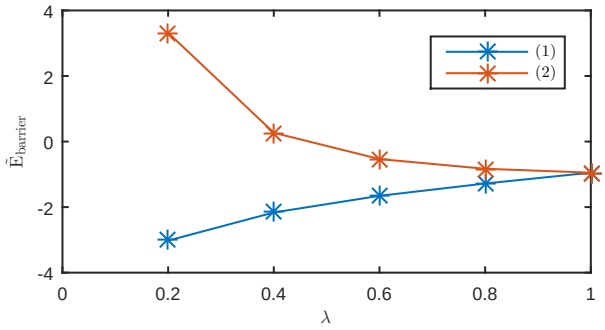

(b) Normalized energy at the saddle points.

Figure 5. The normalized energy for $\lambda = 0.6$, with saddle points indicated by (1) and (2), and the normalized energy at both saddle points in terms of lambda.

branch cut running from $(0, \lambda)$ to (x_1, y_1), the energy can be expressed in terms of line integrals similarly to Equation (8). In the limit as $\epsilon \to 0$, the Oseen–Frank energy is

$$E \sim K\pi \left((1 + m^2) \ln \left(\frac{1}{\epsilon} \right) + \tilde{E}[x_1, y_1, \lambda, m] \right) + O(\epsilon), \tag{26}$$

where the normalized energy $\tilde{E}$ can be evaluated numerically.

To demonstrate an application of this technique, we consider a mechanism for switching between equilibria proposed in [22], in which a corner defect is split into a corner defect of opposing sign and an internal defect of strength $\pm 1/2$, which moves along an edge of Ω. In Figure 5(a), we plot the normalized energy landscape for a rectangular well with $\lambda = 0.6$ and tangent boundary conditions enforced by $a_1 = a_3 = 0$ and $a_2 = a_4 = \frac{\pi}{2}$, with an internal defect of strength $-\frac{1}{2}$. From 5(a), we can identify some features of the normalized energy landscape which occur for all λ. Firstly, the global minimum of $\tilde{E}$ in Ω occurs at the corner at which the internal defect will annihilate

with the corner defect to form the diagonal state, with the boundary data used in Figures 4 and 5(a) this corresponds to the corner at $(0, \lambda)$. Energy minima occur at two further corners of Ω, corresponding to the corners where annihilation of the internal defect will form the U_1 state (at $(0, 0)$) or the U_2 states ($(1, \lambda)$). Secondly, the energy landscape has two critical points, both of which can be identified numerically as saddle points, and therefore states with an internal defect can never be stable equilibria. Finally, there are pathways connecting the D and U_1 states and the D and U_2 states, which minimize the normalized energy required for the internal defect to allow switching between equilibria. The saddle points correspond to maximum values of the normalized energy on these pathways, and have been evaluated for variable λ in Figure 5(b). The saddle point labelled (1) in Figure 5(a) lies on the pathway connecting the D and U_1 states and the saddle point labelled (2) in Figure 5(a) lies on the path connecting the D and U_2 states. The energy at these saddle points represents a measure of the energy barrier between different equilibria, i.e. the minimum energy required for an internal defect to move from one equilibria to another, and can be evaluated using the following formula:

$$E_{\text{barrier}} = \frac{\pi}{4} \ln\left(\frac{1}{\epsilon}\right) + \pi \tilde{E}[x_1^i, y_1^i, \lambda, -1/2] - \pi \tilde{E}_j, \tag{27}$$

where (x_1^i, y_1^i) are the coordinates of the saddle points labelled $i \in \{1, 2\}$ and $j \in \{D, U_i\}$, where $\tilde{E}_j$ are given in Equations (13)–(15).

We conclude this section by giving a brief summary of the empirical estimate for the surface extrapolation length derived in [6]. The experimentalists observe a uniform state with a uniform director profile, $\theta = 0$ on Ω, labelled as the L state. The L state clearly does not respect the tangent boundary conditions on the vertical edges and hence, has an associated energetic cost modelled by the Rapini–Papoular anchoring energy [23]

$$E_L := \oint_{\partial\Omega} \frac{W}{2} \sin^2(\theta - \theta_0)\, \mathrm{d}s, \tag{28}$$

where θ_0 is the preferred director angle on the square edges i.e. $\theta_0 = 0$ on the horizontal edges and $\theta_0 = \frac{\pi}{2}$ on the vertical edges and W is an anchoring coefficient. In [6], the authors use (28) to postulate that the energetic cost of L state originates from the vertical edges and one may observe the L state and the diagonal state simultaneously when

$$E_D = E_L, \tag{29}$$

and E_D is given by (10), as a function of $\lambda = \frac{L_y}{L_x}$. The surface extrapolation length, ξ, is the ratio of the elastic constant K (in the one-constant case, $K_1 = K_2 = K_3 = K$) and the surface anchoring coefficient W [24]. The authors equate the two energies (as in (29)) for values of λ and L_y for which there is experimental coexistence to get

$$\xi := \frac{K}{W} = \frac{L_y}{\pi \ln\left(\frac{2L_y}{\pi\epsilon}\right)}. \tag{30}$$

In other words, they propose a method for estimating a key length scale, the surface extrapolation length, in terms of the geometrical dimensions and a somewhat adhoc small parameter, ϵ, related to the defect core size near each vertex. It is reasonable to assume that ϵ is comparable to the length of a typical molecule but the optimal choice of ϵ in (30) is a matter of speculation.

3. A Two-Dimensional Landau–de Gennes Model

In this section, we summarize the two-dimensional (2D) Landau–de Gennes (LdG) approach in [5, 8] and how it complements the simple Oseen–Frank (OF) approach in [6]. The 2D LdG approach offers three immediate advantages over the OF approach: (i) it includes a scalar order parameter which allows us to track defects, (ii) we can prescribe a single boundary-value problem which admits multiple solutions, including the diagonal and rotated solutions, as opposed to separate boundary-value problems for different equilibria and (iii) consequently, we can track the solution landscape more efficiently as a function of model parameters e.g. λ, material constants, anchoring coefficient, external fields and uncover the unstable solution branches that connect the stable equilibria.

The computational domain is a rectangle as before i.e.

$$\Omega = \left\{(x,y) \in \mathbb{R}^2; x \in [0,L]\,, y \in [0,\lambda L]\right\}, \tag{31}$$

where L is a characteristic length and λ is the rectangular aspect ratio. The $2D$ LdG model describes the nematic state by a 2D LdG $\mathbf{Q}$-tensor order parameter, which is a symmetric, traceless 2×2 matrix with just two degrees of freedom. In particular, it is not as comprehensive as the full LdG theory which describes the nematic state by a symmetric, traceless 3×3 matrix but the $2D$ approach is a natural first step for a largely planar problem, such as the shallow square or cuboid-shaped nematic wells in this paper. The 2D LdG $\mathbf{Q}$-tensor order parameter can be written as

$$\mathbf{Q} = s(x,y)\left(2\boldsymbol{n}\otimes\boldsymbol{n} - \mathbf{I}_2\right), \tag{32}$$

where $\boldsymbol{n}$ is an eigenvector, $s : \Omega \to \mathbb{R}$ is a real scalar order parameter that measures the degree of orientational ordering and $\mathbf{I}_2$ is the 2×2 identity matrix. The eigenvector $\boldsymbol{n}$ can be written in terms of a planar angle, $\theta : \Omega \to \mathbb{R}$ where

$$\boldsymbol{n} = (\cos(\theta(x,y)), \sin(\theta(x,y)))\,, \tag{33}$$

and indeed, one can think of the OF approach as describing the $\boldsymbol{n}$-profiles in (32) without any information about s. In [5], the authors label the 2D LdG $\mathbf{Q}$-tensor by the two matrix components, $\mathbf{Q}_{11}$ and $\mathbf{Q}_{22}$ where

$$\mathbf{Q}_{11} = s\cos(2\theta), \qquad \mathbf{Q}_{12} = s\sin(2\theta). \tag{34}$$

They work with a relatively simple form of the 2D LdG energy, with a bulk potential, an elastic energy density, a surface anchoring energy which is a measure of how strongly the tangent boundary conditions are implemented, and an external field energy and focus on energy minimizers as a function of the anchoring strength and simple switching phenomena mediated by anchoring conditions and electric field. We only reproduce the computations for the field-free case and here, the 2D LdG energy under consideration is

$$\mathcal{E}\left(\mathbf{Q}\right) := \iint_{\Omega} \kappa\left(|\nabla\mathbf{Q}_{11}|^2 + |\nabla\mathbf{Q}_{12}|^2\right) + C\left(\mathbf{Q}_{11}^2 + \mathbf{Q}_{12}^2 - s_0^2\right)^2 \mathrm{d}A + \oint_{\partial\Omega} W\left|(\mathbf{Q}_{11},\mathbf{Q}_{12}) - \boldsymbol{g}\right|^2 \mathrm{d}s, \tag{35}$$

where κ is an elastic constant, $s_0^2 := \frac{|A|}{2C}$ for the rescaled temperature, A, below the nematic supercooling temperature that favours an ordered nematic state and C is a material dependent bulk constant, $\boldsymbol{g} = (g_1, g_2)$ describes the preferred $\mathbf{Q}$-tensor on the boundary and W is a surface anchoring coefficient. There are multiple choices of the surface anchoring energy in the literature but the Durand–Nobili surface energy in (35) offers some numerical advantages, namely (i) the variational problem in (35) is well-posed for all $W > 0$, (ii) the order parameter s is bounded as $W \to \infty$ and (iii) the solutions converge to solutions of a Dirichlet boundary-value problem with

$(\mathbf{Q}_{11}, \mathbf{Q}_{12}) = (g_1, g_2)$ on $\partial\Omega$ as $W \to \infty$ [5], i.e. we recover the Dirichlet boundary conditions as $W \to \infty$. In [5], the authors non-dimensionalize the energy by introducing the rescaled domain, $\tilde{\Omega} := \{(\tilde{x}, \tilde{y}); 0 \leq \tilde{x} \leq 1; 0 \leq \tilde{y} \leq \lambda\}$, $\tilde{x} = \frac{x}{L}, \tilde{y} = \frac{y}{L}$ and the variables

$$\left(\tilde{\mathbf{Q}}_{11}, \tilde{\mathbf{Q}}_{12}\right) = \frac{(\mathbf{Q}_{11}, \mathbf{Q}_{12})}{s_0}, \qquad \tilde{\boldsymbol{g}} = \frac{\boldsymbol{g}}{s_0}, \qquad \tilde{\epsilon} = \frac{1}{L}\sqrt{\frac{\kappa}{C}}, \qquad \tilde{W} = \frac{WL}{\kappa}, \tag{36}$$

and work with

$$\begin{aligned}\frac{1}{s_0^2\kappa}\mathcal{E}[\mathbf{Q}] := \iint_{\Omega} \left(\left|\nabla\tilde{\mathbf{Q}}_{11}\right|^2 + \left|\nabla\tilde{\mathbf{Q}}_{22}\right|^2\right) + \frac{1}{\tilde{\epsilon}^2}\left(\tilde{\mathbf{Q}}_{11}^2 + \tilde{\mathbf{Q}}_{12}^2 - 1\right)^2 \mathrm{d}\tilde{A} \\ + \oint_{\partial\tilde{\Omega}} \tilde{W}\left|\left(\tilde{\mathbf{Q}}_{11}, \tilde{\mathbf{Q}}_{12}\right) - \tilde{\boldsymbol{g}}\right|^2 \mathrm{d}\tilde{s},\end{aligned} \tag{37}$$

where $\mathrm{d}\tilde{A}$ and $\mathrm{d}\tilde{s}$ are the rescaled area and length element respectively. In what follows, we drop the tildes for brevity, fix $\epsilon = 0.02$ and study LdG energy minimizers, or locally stable equilibria, as a function of the rescaled anchoring coefficient, W.

The tangent boundary conditions require that $\boldsymbol{n} = \pm\hat{\boldsymbol{x}}$ on $y = 0, y = \lambda$ and $\boldsymbol{n} = \pm\hat{\boldsymbol{y}}$ on $x = 0, 1$ so that

$$\begin{aligned}&\mathbf{Q}_{11} \geq 0 \quad \text{on horizontal edges,} \\ &\mathbf{Q}_{11} \leq 0 \quad \text{on vertical edges,} \\ &\mathbf{Q}_{12} = 0 \quad \text{on } \partial\Omega.\end{aligned} \tag{38}$$

The authors define *optimal boundary conditions* in [5] by solving the following variational problem in weak form

$$0 = \int_{\Omega} \nabla\mathbf{Q}_{11} \cdot \nabla v_{11} + \frac{2}{\epsilon^2}\left(\mathbf{Q}_{11}^2 + \mathbf{Q}_{12}^2 - 1\right)\mathbf{Q}_{11} v_{11}\,\mathrm{d}A \qquad \forall v_{11} \in H^1(\Omega), \tag{39}$$

$$0 = \int_{\Omega} \nabla\mathbf{Q}_{12} \cdot \nabla v_{12} + \frac{2}{\epsilon^2}\left(\mathbf{Q}_{11}^2 + \mathbf{Q}_{12}^2 - 1\right)\mathbf{Q}_{12} v_{12}\,\mathrm{d}A \qquad \forall v_{12} \in H_0^1(\Omega), \tag{40}$$

i.e. this formulation only includes the constraint $\mathbf{Q}_{12} = 0$ on $\partial\Omega$ and $\mathbf{Q}_{11}$ is left free[1] . In [5], the authors numerically find six solutions for the integral equations (39)–(40) for $\epsilon = 0.02$, two diagonal solutions and four rotated solutions and label the corresponding solutions as *optimal solutions* and their traces on $\partial\Omega$ as *optimal boundary conditions*. These solutions are optimal in the sense that they are the minimal energy solutions in their respective class. In other words, there are multiple diagonal solutions consistent with (38) and the optimal diagonal solution is the minimal energy diagonal solution consistent with (38). We point out that all optimal boundary conditions vanish at the square vertices i.e. $\mathbf{Q} = 0$ at the vertices or, equivalently, we have point defects at the vertices which arise naturally from the mismatch in the tangent orientations at the vertices.

The concept of optimal boundary conditions is both novel and insightful because it yields quantitative information about how to select the best boundary conditions as a function of ϵ, which is a material- and geometry-dependent parameter. In what follows, the authors take the optimal diagonal boundary condition as the preferred orientation, $\boldsymbol{g}$, in (37). The next step is to compute static equilibria or stable critical points of (37) as a function of the re-scaled anchoring coefficient W. We reproduce Figure 6 from [5]; the authors use finite-element methods to solve the weak

[1]The integral equations in (39) and (40) are the weak form for the Euler–Lagrange equations for 2D LdG equilibria that have $\mathbf{Q}_{12} = 0$ on the boundary and this is the standard form used by numerical analysts.

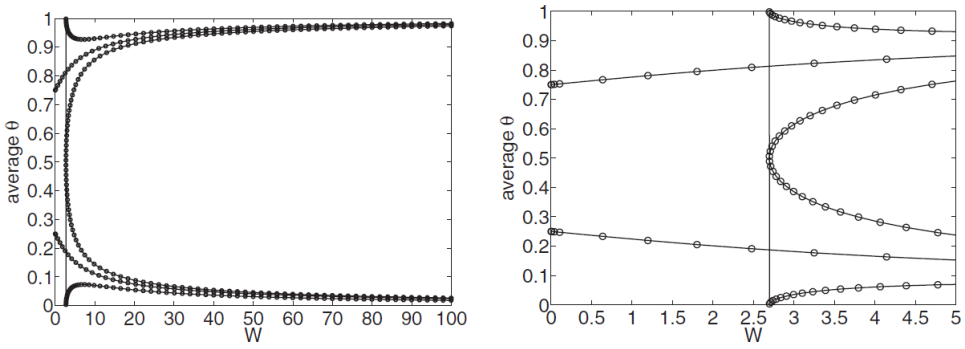

(a) The whole picture.

(b) Zoom-in near the critical anchoring strength.

Figure 6. The bifurcation diagram. Parameters: $\epsilon = 0.02$, mesh size $N = 32$, and $a_r = 1$. Reproduced from [5] with permission of the American Physical Society.

form of the Euler-Lagrange equations associated with (37) and trace the solution branches using pseudo-arc-length continuation [25]. In Figure 6, the diagonal solutions are stable for all $W \geq 0$ and degenerate to a constant solution with $\mathbf{Q}_{11} = 0, \mathbf{Q}_{12} = \pm 1$ at $W = 0$. At $W = 0$, the tangent boundary conditions are not implemented. The rotated solutions are stable only above a critical threshold, $W = W_c$, and the numerical methods in [5] cannot track unstable solution branches. At $W = W_c$, the rotated solution either degenerate into a profile with $\mathbf{Q}_{11} = 1, \mathbf{Q}_{12} = 0$ in the square interior with transition layers near the vertical edges, or into a profile with $\mathbf{Q}_{11} = -1, \mathbf{Q}_{12} = 0$ in the square interior with transition layers near the horizontal edges. These transition layers are energetically expensive for a finite W and hence, it is reasonable to argue that rotated branches are unstable for $W < W_c$. The numerical investigations in [5] suggest the following empirical relation between W_c and ϵ:

$$W_c(\epsilon) = 2.54 + 10.30\epsilon, \tag{41}$$

which again defines a quantitative relation between material properties, geometry and anchoring conditions.

In [8], the authors build on the work in [5] with emphasis on the free energy landscape and the transient states that connect stable equilibria given by local LdG energy minimizers. The authors use a combination of the doubly-nudged elastic band (DNEB) method and the hybrid eigenvector-following technique [26] to compute transition states which are special saddle points or critical points of the LdG energy for which the energy gradient is zero in all eigendirections and the Hessian has a single negative eigenvalue. By contrast, a local energy minimizer has zero energy gradient in all eigendirections and the Hessian has positive eigenvalues. The authors work with $\epsilon = 0.02$ in (37) and distinguish between three regimes labelled by a re-scaled anchoring coefficient, $W = \frac{W_s}{\alpha L}$ where W_s is the anchoring coefficient, $\alpha = |A|$ is a measure of the temperature (fixed in [8]) and L is the fixed square length. The authors work with (i) strong anchoring labelled by $W \geq 6.5 \times 10^{-3}$, (ii) moderate anchoring for which $1.4 \times 10^{-3} \leq W \leq 6.5 \times 10^{-3}$ and (iii) weak anchoring labelled by $W < 1.4 \times 10^{-3}$.

For strong anchoring, the authors find the conventional diagonal and rotated solutions, and each diagonal and rotated solution is connected by a transition state. It is noteworthy that the authors do not find a direct pathway between pairs of diagonal solutions or pairs of rotated solutions. We reproduce Figure 7 from [8] which illustrate two of the transition states in the strong anchoring regime. There are multiple transition pathways but the optimal transition pathway has the minimum energy barrier with the transition state located at the maximum of the energy profile. In Figure 7(a)–(c), the transition state, connecting a rotated to a diagonal solution, is distinguished by a $-1/2$-defect near the centre of the left vertical edge and the entire transition pathway is mediated

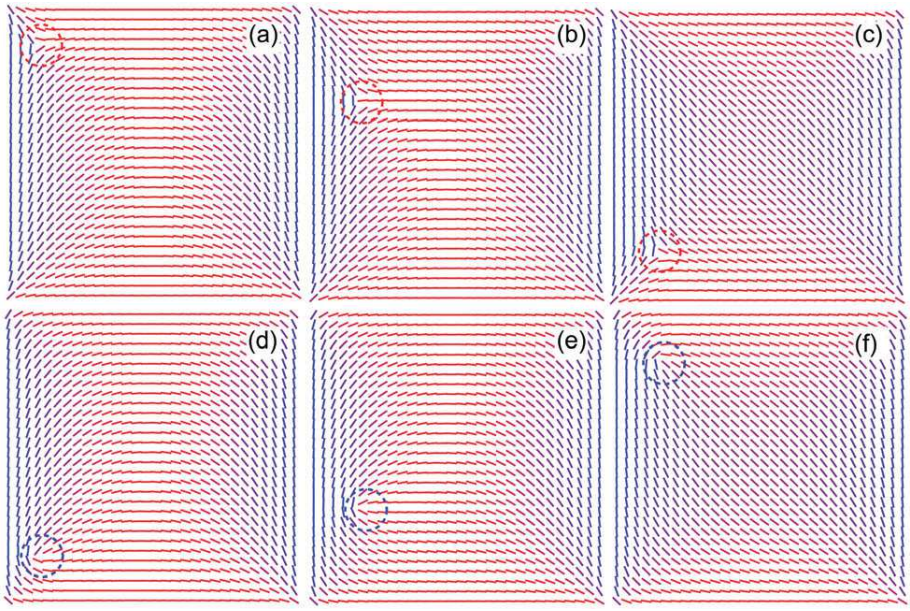

Figure 7. Possible transition pathways between rotated and diagonal states in the strong anchoring limit, $W \geq 6.5 \times 10^{-3}$. The transitions are mediated by a $-1/2$ defect in panels (a)–(c) and a $+1/2$ defect in (d)–(f). Adapted from [8] with permission of the Royal Society of Chemistry.

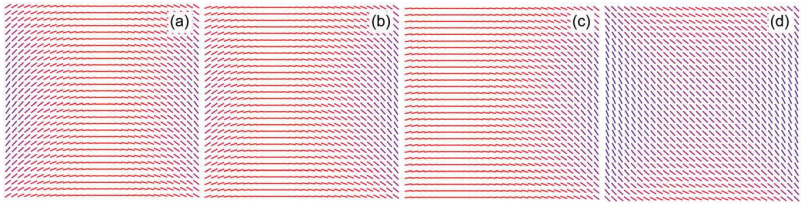

Figure 8. The optimal transition pathway between a rotated (panel a) and a diagonal state (panel d) in the medium anchoring regime, $1.4 \times 10^{-3} \leq W \leq 2.4 \times 10^{-3}$. Panel (b) corresponds to the transition state, while panel (c) is an intermediate state along the pathway. Reproduced from [8] with permission of the Royal Society of Chemistry.

by the motion of a $-1/2$ defect from the top left vertex towards the bottom left vertex, following the edge length. There is at least one other optimal transition pathway mediated by the motion of a $+1/2$ defect from the bottom left vertex towards the top left vertex, achieving a rotated to diagonal transition as before (Figure 7(d)–(f)).

The moderate anchoring regime has different qualitative features. The transition pathways do not feature defects but are rather mediated by localized anchoring breaking along an entire edge. We reproduce Figure 8 from [8], the director rotates clockwise near the bottom left vertex, breaks the tangential anchoring near the bottom left vertex and the rotation propagates upwards, facilitating the rotated to diagonal transition. For weaker anchoring in the moderate parameter regime, the rotated to diagonal transition is mediated by *global director rotation* along the entire length of the edge, breaking the tangential anchoring along the edge. In such cases, it is energetically preferable to break the tangential anchoring along an edge as opposed to the creation of interior defects or defects along an edge. In the weak anchoring regime, the rotated solutions are not stable consistent with the bifurcation diagram in Figure 6. Instead, the rotated solutions act as transition states connecting the stable diagonal solutions as demonstrated in Figure 9. The rotated profile in this regime, though unstable, has an almost uniform profile in the interior with a pair of localised transition layers near the edges, reminiscent of the limiting profiles near $W = W_c$ in Figure 6.

In Figure 10, the authors plot the energy profiles along the optimal transition pathways as a function of the anchoring strength. In the strong anchoring regime, the energy profile is almost

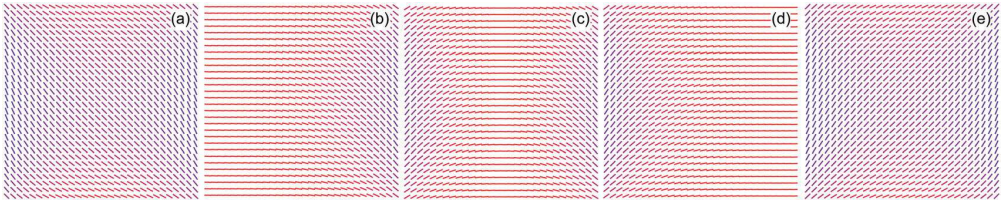

Figure 9. One of four equivalent optimal transition pathways between two diagonal states (panels a and e) in the weak anchoring regime, $W \leq 1.4 \times 10^{-3}$. Panel (c) corresponds to the transition state, which is reminiscent of a rotated state. Panels (b) and (d) are intermediate states along the pathway. Reproduced from [8] with permission of the Royal Society of Chemistry.

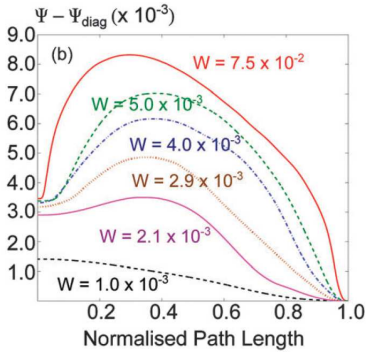

Figure 10. The free energy profiles along the optimal transition pathway for different values of the surface anchoring strength W. Adapted from [8] with permission of the Royal Society of Chemistry.

independent of W. In the moderate and weak anchoring regimes, the energy barrier decreases almost monotonically with decreasing W.

The work in [8] takes the framework in [5] further by a comprehensive study of the LdG solution landscape as a function of the anchoring coefficient W, including energy minima, transition states, transition pathways and free energy barriers. The transition states in the strong anchoring regimes, distinguished by $\pm 1/2$ defects, are strongly reminiscent of recent experimental observations [20] and hence, are of physical relevance in spite of being unstable LdG critical points. Further, the energy barrier computations are relevant for the stability of liquid crystal systems and switching mechanisms. A high energy barrier can be an impedance to switching and we need strong external fields to induce diagonal to rotated switching and vice-versa in such regimes. Alternatively, a small energy barrier compromises the stability and robustness of a confined system. One of the primary goals of such computational exercises is to find the best combination of material parameters, geometry, anchoring conditions and in some cases, external fields, for optimal performance and minimum operational costs. In [5, 8], all parameters are essentially fixed with the exception of the anchoring coefficient and in the final section, we illustrate the interplay between square size, anchoring coefficient and temperature in a 3D LdG framework.

4. A 3D Landau–de Gennes Approach

In [7], the authors employ a 3D LdG modelling approach and numerically discover a new well order reconstruction solution (WORS) for small wells or wells with cross-sectional parameters comparable to the biaxial correlation length. We briefly describe their results below.

The computational domain is a 3D well with a square cross-section, $\mathcal{B} \subset \mathbb{R}^3$, defined by

$$\mathcal{B} = \left\{(x, y, z) \in \mathbb{R}^3; 0 \leq x, y \leq R, 0 \leq z \leq h\right\}, \tag{42}$$

where $h = \frac{R}{10}$ by assumption. The coordinate unit-vectors are denoted by $\hat{\boldsymbol{x}}$, $\hat{\boldsymbol{y}}$, $\hat{\boldsymbol{z}}$ in the x, y, z directions respectively. In [7], the authors work with a 3D LdG order parameter: the full LdG $\mathbf{Q}$-tensor order parameter described by a symmetric, traceless 3×3 matrix with five degrees of freedom as shown below:

$$\mathbf{Q} = \sum_{i=1}^{3} \lambda_i \boldsymbol{e}_i \otimes \boldsymbol{e}_i, \tag{43}$$

where $\boldsymbol{e}_i$ denote the eigenvectors or preferred directions, the λ_i's are the corresponding eigenvalues that measure the degree of order about these directions and $\sum_i \lambda_i = 0$. A $\mathbf{Q}$-tensor is (i) isotropic if $\mathbf{Q} = 0$, (ii) uniaxial if there are two equal non-zero eigenvalues so that there is a single distinguished eigendirection with the non-degenerate eigenvalue, analogous to the director in the OF framework and (iii) biaxial if there are three distinct eigenvalues. In particular, biaxiality is outside the scope of the OF and 2D LdG approaches described in the preceding sections. The biaxiality parameter, β^2, is defined to be

$$\beta^2 := 1 - \frac{6\left(\mathrm{tr}\mathbf{Q}^3\right)^2}{|\mathbf{Q}|^6}, \tag{44}$$

where $\mathrm{tr}\mathbf{Q}^3 = \sum_{i=1}^{3} \lambda_i^3$, $|\mathbf{Q}|^2 = \sum_{i=1}^{3} \lambda_i^2$ and $\beta^2 \in [0,1]$ with $\beta^2 = 0$ if and only if $\mathbf{Q}$ is uniaxial [27]. Maximal biaxiality, $\beta^2 = 1$, occurs when $\mathbf{Q}$ has a zero eigenvalue.

The 3D LdG energy functional differs from the 2D energy in Section 3 above. In [7], the authors work with

$$I[\mathbf{Q}] := \iiint_{\mathcal{B}} f_B\left(\mathbf{Q}\right) + f_E\left(\mathbf{Q}, \nabla\mathbf{Q}\right)\ dV + \oint_{\partial\mathcal{B}} f_s(\mathbf{Q}, \mathbf{Q}_s^i)\,\mathrm{d}A \tag{45}$$

where

$$\begin{aligned} f_B\left(\mathbf{Q}\right) &:= \frac{A_0\left(T - T^*\right)}{2}\mathrm{tr}\mathbf{Q}^2 - \frac{B}{3}\mathrm{tr}\mathbf{Q}^3 + \frac{C}{4}\left(\mathrm{tr}\mathbf{Q}^2\right)^2, \\ f_E\left(\mathbf{Q}, \nabla\mathbf{Q}\right) &:= \frac{L}{2}\left|\nabla\mathbf{Q}\right|^2, \qquad f_s(\mathbf{Q}, \mathbf{Q}_s^i) := \frac{W^i}{2}\left|\mathbf{Q} - \mathbf{Q}_s^i\right|^2, \end{aligned} \tag{46}$$

A_0, B, C are fixed material-dependent constants, T^* is a characteristic nematic supercooling temperature, L is a fixed elastic constant, W^i is the anchoring coefficient on the i^{th} boundary surface ($\mathcal{B}$ has six boundaries: the faces $x = 0, R$, $y = 0, R$, $z = 0, h$) and $\mathbf{Q}_s^i$ is the preferred $\mathbf{Q}$-tensor on the i-th bounding surface. The bulk potential f_B in (46) only admits either uniaxial or isotropic critical points [2, 28, 29] and the isotropic state is an unstable critical point for $T < T^*$. In [7], the authors work with temperatures, $T < T^*$, for which f_B admits uniaxial critical points

$$\mathbf{Q}_{\min} = S_{eq}(T)\left(\boldsymbol{m} \otimes \boldsymbol{m} - \frac{\mathbf{I}}{3}\right), \tag{47}$$

for arbitrary $\boldsymbol{m} \in S^2$ and $S_{eq}(T) = \frac{B + \sqrt{B^2 + 24|A|C}}{4C}$. In what follows, the authors work with free boundary conditions on $z = 0$ and $z = h$ and prescribe $\mathbf{Q}_s^i$ on the lateral surfaces as given below:

$$\begin{aligned} \mathbf{Q}_s^x &= \frac{S_{eq}}{3}\left(2\hat{\boldsymbol{y}} \otimes \hat{\boldsymbol{y}} - \hat{\boldsymbol{x}} \otimes \hat{\boldsymbol{x}} - \hat{\boldsymbol{z}} \otimes \hat{\boldsymbol{z}}\right) \qquad x = 0 \text{ and } x = R, \\ \mathbf{Q}_s^y &= \frac{S_{eq}}{3}\left(2\hat{\boldsymbol{x}} \otimes \hat{\boldsymbol{x}} - \hat{\boldsymbol{y}} \otimes \hat{\boldsymbol{y}} - \hat{\boldsymbol{z}} \otimes \hat{\boldsymbol{z}}\right) \qquad y = 0 \text{ and } y = R. \end{aligned} \tag{48}$$

The conditions (48) naturally create line defects along the vertical edges but since W^i is finite, the energy minimizers can break the tangential anchoring along the vertical edges and eliminate the associated line defects. Further, the assumed free boundary conditions on $z = 0$ and $z = h$ are an alternative means of imposing planar degenerate conditions on these surfaces with no preferred in-plane orientation. The numerical results in [7] suggest that the static equilibria (in this particular modelling framework) are indeed invariant in the z-direction so that it suffices to look at the LdG $\mathbf{Q}$-tensor profile on the bottom cross-section $z = 0$.

In [7], the authors adopt a particular parameterization of the LdG $\mathbf{Q}$-tensor

$$\mathbf{Q} := (q_3 + q_1)\,\hat{\boldsymbol{x}} \otimes \hat{\boldsymbol{x}} + (q_3 - q_1)\,\hat{\boldsymbol{y}} \otimes \hat{\boldsymbol{y}} + q_2\,(\hat{\boldsymbol{x}} \otimes \hat{\boldsymbol{y}} + \hat{\boldsymbol{y}} \otimes \hat{\boldsymbol{x}}) - 2q_3\hat{\boldsymbol{z}} \otimes \hat{\boldsymbol{z}}, \tag{49}$$

where q_1, q_2, q_3 are assumed to be independent of the z-coordinate. We note that $\mathbf{Q}$ has a constant eigenframe if $q_2 = 0$ and maximal biaxiality if $q_1 = q_2 = 0$. The authors measure R relative to a material-dependent and temperature-dependent length scale, known as the bare biaxial correlation length

$$\xi_b^{(0)} := \frac{2\sqrt{LC}}{B}, \tag{50}$$

and the biaxial correlation length in the literature [27, 30]:

$$\xi_b := \frac{\xi_b^{(0)}}{\sqrt{1 + \sqrt{\tau}}} \tag{51}$$

where $\tau := 1 - \frac{T - T_*}{T_{**} - T_*}$, T_{**} is another critical temperature such that $\mathbf{Q} = 0$ is the isolated critical point of f_B for $T > T_{**}$. The anchoring strength is measured in terms of the surface extrapolation length, denoted by

$$d^i = \frac{L}{W^i}, \tag{52}$$

on each of the lateral surfaces. In [7], the authors numerically solve the Euler-Lagrange equations associated with (45) by using relaxation methods [31, 32], that compute static equilibria by following a gradient-flow like procedure along which the energy continuously decreases till equilibrium is attained, for different initial conditions. The numerically computed static equilibria are robust with respect to different choices of the initial conditions and are hence, numerically stable.

For any fixed value of τ, the authors find a unique WORS for well sizes, $\eta = \frac{R}{\xi_b^{(0)}} \leq \eta_c(\tau, W^i)$ where the critical value η_c depends on both the temperature and the anchoring strength on the four lateral surfaces, W^i. The authors assume equal anchoring strength on the lateral surfaces and set $W = W^i$. The WORS is distinctive in the sense that $q_2 = 0$ throughout the $z = 0$ cross-section in (49) and $q_1 = 0$ along the square diagonals. Notably, this implies that $\beta^2 = 0$ along the square diagonals and

$$\mathbf{Q} = -q_3\,(2\hat{\boldsymbol{z}} \otimes \hat{\boldsymbol{z}} - \hat{\boldsymbol{x}} \otimes \hat{\boldsymbol{x}} - \hat{\boldsymbol{y}} \otimes \hat{\boldsymbol{y}}) \quad \text{on } x = \pm y, \tag{53}$$

where $q_3 > 0$ from numerical simulations i.e. $\mathbf{Q}$ is uniaxial with negative scalar order parameter along the square diagonals. The uniaxial diagonal cross is surrounded by a star-shaped ring of maximal biaxiality with $\beta^2 = 1$ and this maximally biaxial ring separates the uniaxial diagonal cross with negative scalar order parameter from the uniaxial edge states with positive order parameter (see the definition of $\mathbf{Q}_s^i$ in (48)). The authors refer to this new solution as the WORS by analogy with other examples of order reconstruction phenomena in [33–35] where the LdG critical point connects a negatively ordered and a positively ordered uniaxial state via a maximally biaxial state.

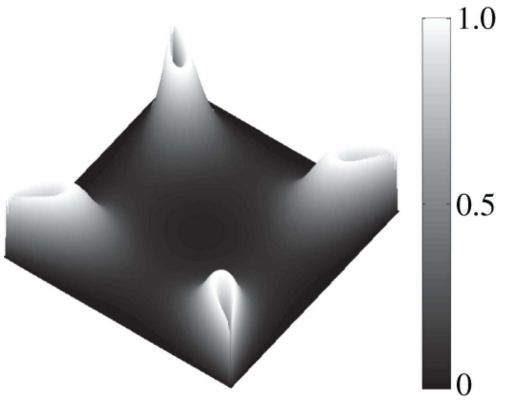

Figure 11. The degree of biaxiality, $\beta^2(x,y)$, in a square well with $R/\xi_b^{(0)} = 4.5$, $\tau = 4$ and strong anchoring conditions. The shading code for $\beta^2 \in [0,1]$ is on the right side. Reproduced from [7] with permission of the Royal Society.

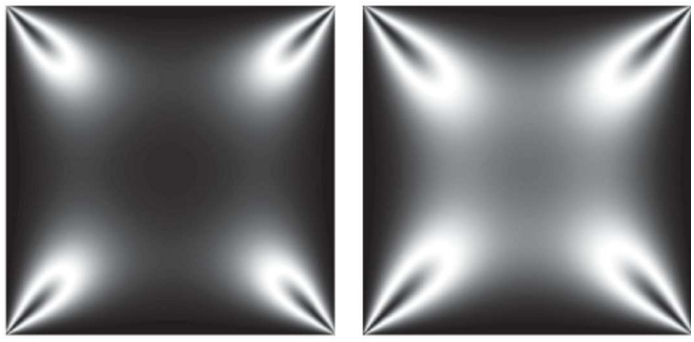

(a) $\eta = 4.5$. (b) $\eta = 3.8$.

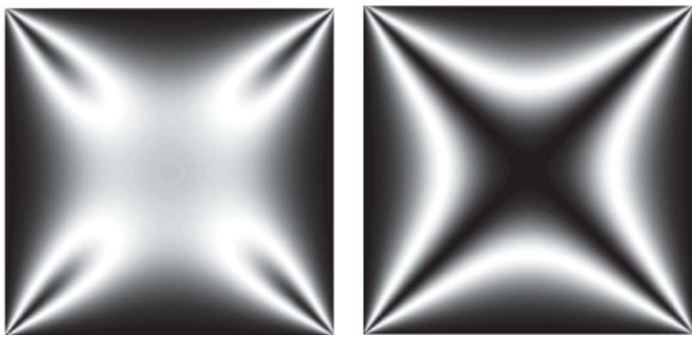

(c) $\eta = 3.6$ (d) $\eta = 3$.

Figure 12. The degree of biaxiality, $\beta^2(x,y)$, in a square well with $R/\xi_b^{(0)} = 4.5$, $\tau = 4$and strong anchoring conditions. We observe the WORS below the critical value $\eta_c = 3.28 \mp 0.01$. Reproduced from [7] with permission of the Royal Society.

The WORS is different from previously reported order reconstruction solutions since it is fully two-dimensional and is the unique LdG critical point, and hence, the physically relevant LdG critical point, for small wells.

We reproduce Figures 11, 12, 13, 14 from [7] which illustrate the biaxiality profile of both the diagonal solution and the WORS along with the dependence of η_c on both τ and W. The diagonal solution is predominantly uniaxial with $\beta^2 \approx 0$, with the exception of small biaxial lobes localized near the vertices and it is reasonable to expect the conventional diagonal solution and the new WORS to have different optical properties. It is clear that η_c is an increasing function of temperature so that the WORS can be more effectively stabilized for higher temperatures. Further, for

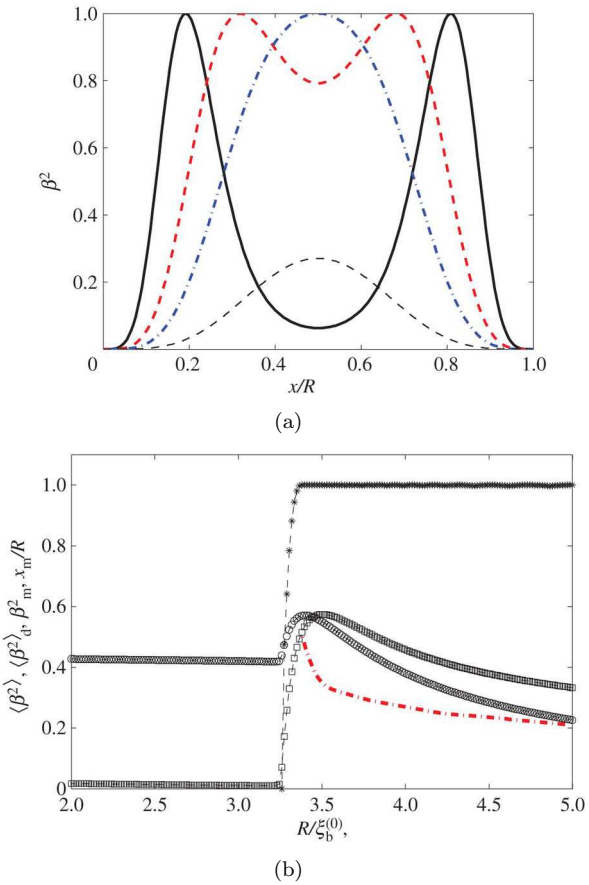

Figure 13. Onset of the WORS with $\tau = 4$ and strong anchoring conditions. (a) Plots of $\beta^2(x)$ along the well diagonal, where x/R is the scaled distance along the square diagonal measured from the bottom left vertex. $\beta = 4.5$, thick full line; $\beta = 3.5$, thick dashed line; $\beta = 3.39$, thick dash-dash line; $\beta = 3.3$, thin dashed line with maximum at $\beta^2 < 0.5$. (b) Structural characteristics of WORS: $\langle\beta^2\rangle_d$ (open squares), $\langle\beta^2\rangle$ (open spheres), β_m^2 (asterisks) and x_m (dashed line) as a function of β. The WORS is defined by $R = R_c$ for which $\beta_m^2 = \langle\beta^2\rangle_d = 0$, $\beta_m^2 = 0$ for $R < R_c$ and x_m is not defined for $\eta < \eta_c$. Reproduced from [7] with permission of the Royal Society.

a given τ, η_c quickly approaches an asymptotic value as W increases, referred to as the strong anchoring value. However, η_c decreases sharply as W decreases so that the WORS may not be observable for weakly anchored systems. This is not surprising since the WORS is a consequence of the conflicting preferred tangential orientations on the square edges and if these orientations are "weakly" preferred, it is energetically preferable for the nematic system to violate the preferred tangent conditions and adopt a more uniform state throughout $z = 0$ at a lower energy cost. It remains a challenge to engineer experimental conditions that would realize the WORS.

5. Conclusions

In this paper, we review three different modelling approaches for NLC-filled square or cuboid-shaped wells with tangent boundary conditions, used in a batch of four recent papers [5–8]. In Section 2, we work with the simplest 2D OF approach. This simple model cannot describe the singular profiles near the defects but works well for an average description of the diagonal and rotated solutions for large micron-scale wells, and can be extended to include the effects of internal defects. The $2D$ LdG approach in Section 3 is an improvement over the OF model since it contains an order parameter, s, which vanishes at defects i.e. $s = 0$ at the well vertices for the experimentally observed equilibria. In fact, one could think of the $2D$ LdG approach as being a weighted OF

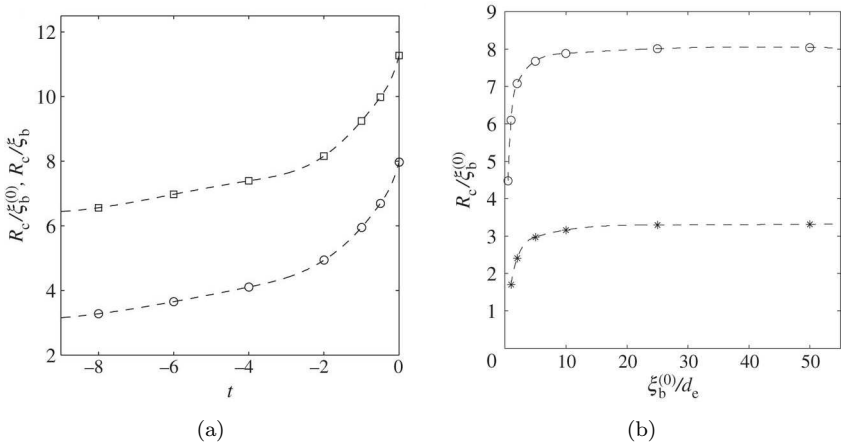

Figure 14. Effect of temperature and anchoring strength on the stability of WORS. Symbols designate points where thresholds are calculated. Lines are guides for the eye. (a) Temperature variation of $\eta_c = \sqrt{\tau}\eta_c = R_c/\xi_b$ (squares) and $\eta_c = Rc/\xi_b^{(0)}$ (spheres) with strong anchoring condition. (b) Impact of anchoring strength on η_c for $t = -8$ (asterisk symbols) and $t = 0$ (spheres). Reproduced from [7] with permission of the Royal Society.

model, for which the director $\boldsymbol{n}$ is weighted by a regularizing order parameter. We work with a fixed small value of $\epsilon = 0.02$ in (37), which coerces energy minimizers to have fixed norm, $\mathbf{Q}_{11}^2 + \mathbf{Q}_{22}^2 = s_0^2$, almost everywhere except near defects. In fact, it is reasonable to think of the $\epsilon \to 0$ limit as being the Oseen–Frank limit [36], since the qualitative predictions of a sophisticated LdG theory effectively reduce to OF predictions away from singularities in this asymptotic limit. Therefore, it is not surprising that we effectively recover the diagonal and rotated solutions for small ϵ in the 2D LdG framework with additional information about the order profiles near the defects [5]. Additionally, we reproduce numerical results from [5, 8] where stable solution branches and transient states are tracked as a function of the anchoring coefficient in the 2D LdG framework. It is perfectly feasible that one might obtain similar results by studying the 2D OF model with a Rapini-Papoular surface energy and indeed in [9], the author makes progress on these lines. Of course, the 2D LdG approach also allows us to track order parameter variations as a function of anchoring strength, which is outside the scope of an OF model. In Section 4, we review the work in [7] and use a full 3D LdG approach to model the NLC-filled square wells. There are some underpinning assumptions, for example the variables q_1, q_2, q_3 in (49) are assumed to be independent of z. The 3D approach accounts for biaxiality, which is outside the scope of the OF and 2D LdG approaches. Indeed, this 3D approach reveals the biaxial nature of the defect profiles near the square vertices (see Figure 12) for a diagonal solution. Equally importantly, this modelling approach shows that for a fixed temperature and anchoring strength, there is a critical well size such that there is a unique WORS for all wells smaller than the critical size. The WORS is distinguished by a uniaxial diagonal cross of negative scalar order parameter surrounded by a star-shaped ring of maximal biaxiality. In [37], the authors provide an analytic description of the numerically reported WORS (also see [38] for an analysis of a one-dimensional order reconstruction problem and general uniqueness result for elliptic PDEs for small domain sizes) and in [19], the authors study the 3D LdG solution landscape as a function of the well size, at fixed temperature and anchoring conditions. The WORS loses stability and the instability is accompanied by two stable "diagonal" solution branches and two unstable "rotated" branches, which eventually bifurcate into 4 stable rotated solution branches. A lot remains to be understood about the bifurcation diagram and these questions will be pursued in future work.

Acknowledgements

The authors are grateful to Oliver Dammone, Peter Howell, Dirk Aarts, Halim Kusumaatmaja, Radek Erban, Chong Luo and Samo Kralj for fruitful discussions and suggestions. In compliance with EPSRCs open access initiative, the data in Figure 5 and the MATLAB codes which generated it, are available from http://dx.doi.org/xxx/xxx.

Funding

A.M. is supported by an EPSRC Career Acceleration Fellowship EP/J001686/1 and EP/J001686/2, an OCIAM Visiting Fellowship, support from the Bath Internationalization Grant schemes and the Bath Institute for Mathematical Innovation. A.L. is supported by an Engineering Physical Sciences Research Council studentship.

References

[1] de Gennes PG. The Physics of Liquid Crystals. Oxford: Clarendon Press; 1974.
[2] Virga EG. Variational Theories for Liquid Crystals. London: Chapman and Hall; 1994.
[3] Bahadur B. Liquid crystals: applications and uses. World Scientific; 1991.
[4] Lagerwall JPF. An introduction to the physics of liquid crystals. In: Fernandez-Nieves A, editor. Soft materials - generation, physical properties and fundamental applications. John Wiley & Sons; 2014.
[5] Luo C, Majumdar A, Erban R. Multistability in planar liquid crystal wells. Phys Rev E. 2012 Jun; 85:061702.
[6] Lewis AH, Garlea I, Alvarado J, Dammone OJ, Howell PD, Majumdar A, Mulder BM, Lettinga MP, Koenderink GH, Aarts DGAL. Colloidal liquid crystals in rectangular confinement: theory and experiment. Soft Matter. 2014;10:7865–7873.
[7] Kralj S, Majumdar A. Order reconstruction patterns in nematic liquid crystal wells. Proc R Soc A. 2014;470(2169):20140276.
[8] Kusumaatmaja H, Majumdar A. Free energy pathways of a multistable liquid crystal device. Soft Matter. 2015;11:4809–4817; Available from: h.
[9] Lewis AH. Defects in liquid crystals: Mathematical and experimental studies [dissertation]. University of Oxford; 2016.
[10] Raisch A, Majumdar A. Order reconstruction phenomena and temperature -driven dynamics in a 3D zenithally bistable device. EPL. 2014;107(1):16002.
[11] Kitson S, Geisow A. Controllable alignment of nematic liquid crystals around microscopic posts: Stabilization of multiple states. Appl Phys Lett. 2002;80(19):3635–3637.
[12] Majumdar A, Newton CJP, Robbins JM, Zyskin M. Topology and bistability in liquid crystal devices. Phys Rev E. 2007 May;75:051703.
[13] Spencer T, Care C, Amos R, Jones J. Zenithal bistable device: Comparison of modeling and experiment. Physical Review E. 2010;82(2):021702.
[14] Robbins J, Zyskin M. Classification of unit-vector fields in convex polyhedra with tangent boundary conditions. Journal of Physics A: Mathematical and General. 2004;37(44):10609.
[15] Tsakonas C, Davidson AJ, Brown CV, Mottram NJ. Multistable alignment states in nematic liquid crystal filled wells. Appl Phys Lett. 2007;90(11):111913.
[16] Evans C, Davidson A, Brown C, Mottram N. Static alignment states in a bistable azimuthal nematic device with blazed grating sidewalls. Journal of Physics D: Applied Physics. 2010;43(49):495105.
[17] Anquetil-Deck C, Cleaver DJ, Atherton TJ. Competing alignments of nematic liquid crystals on square-patterned substrates. Physical Review E. 2012;86(4):041707.
[18] Yakutovich M, Newton C, Cleaver D. Mesh-free simulation of complex lcd geometries. Molecular crystals and liquid crystals. 2009;502(1):245–257.
[19] Robinson M, Luo C, Erban R, Majumdar A. Nematic square wells: molecular and macroscopic studies. In preparation. 2016;.

[20] Dammone OJ. Confinement of colloidal liquid crystals [dissertation]. University College, University of Oxford; 2013.
[21] Van Loan CF, Fan KYD. Insight through computing: a MATLAB introduction to computational science and engineering. SIAM; 2010.
[22] Davidson AJ, Mottram NJ. Conformal mapping techniques for the modelling of liquid crystal devices. Eur J Appl Math. 2012;23:99–119.
[23] Barbero G, Durand G. On the validity of the Rapini-Papoular surface anchoring energy form in nematic liquid crystals. J de Phys. 1986;47(12):2129–2134.
[24] Allen MP. Molecular simulation and theory of liquid crystal surface anchoring. Mol Phys. 1999; 96(9):1391–1397.
[25] Seydel R. Practical bifurcation and stability analysis. Vol. 5. Springer Science & Business Media; 2009.
[26] Kusumaatmaja H. Surveying the free energy landscapes of continuum models: Application to soft matter systems. J Chem Phys. 2015;142(12):124112.
[27] Kralj S, Virga EG. Universal fine structure of nematic hedgehogs. J Phys A: Math Gen. 2001;34(4):829.
[28] Majumdar A. Equilibrium order parameters of nematic liquid crystals in the Landau-de Gennes theory. Eur J Appl Math. 2010 4;21:181–203.
[29] Ball JM. Function spaces for liquid crystals. 2015 Dec; winter school, Nonlinear Function Spaces in Mathematics and Physical Sciences, Lyon; Available from: https://people.maths.ox.ac.uk/ball/Teaching/lyon2015.pdf.
[30] Ambrožič M, Bisi F, Virga EG. Director reorientation and order reconstruction: competing mechanisms in a nematic cell. Contin Mech Thermodyn. 2008;20(4):193–218.
[31] Kralj S, Virga EG, Žumer S. Biaxial torus around nematic point defects. Phys Rev E. 1999;60(2):1858.
[32] Press WH, Flannery BP, Teukolsky S, Vetterling WT. Numerical recipes. 1986. Cambridge University Press, Cambridge; 1986.
[33] Biscari P, Peroli GG, Sluckin T. The topological microstructure of defects in nematic liquid crystals. Molecular Crystals and Liquid Crystals. 1997;292(1):91–101.
[34] Mkaddem S, Gartland Jr EC. Fine structure of defects in radial nematic droplets. Phys Rev E. 2000; 62(5):6694.
[35] Palffy-Muhoray P, Gartland E, Kelly J. A new configurational transition in inhomogeneous nematics. Liquid Crystals. 1994;16(4):713–718.
[36] Majumdar A, Zarnescu A. Landau-de Gennes theory of nematic liquid crystals: the Oseen-Frank limit and beyond. Arch Rational Mech Anal. 2010;196(1):227–280.
[37] Canevari G, Spicer A, Majumdar A. The order reconstruction solution for nematic square wells: A variational atudy. In preparation. 2016;.
[38] Lamy X. Bifurcation analysis in a frustrated nematic cell. Journal of Nonlinear Science. 2014;24(6):1197–1230.